Supporting Information for "Experimental multiblast craters and ejecta"

DOI: 10.1002/...

Ingo Sonder[1], Alison Graettinger[2], Tracianne B. Neilsen[3], Robin S. Matoza[4], Jacopo Taddeucci[5], Julie Oppenheimer[6], Einat Lev[6], Kae Tsunematsu[7], Greg Waite[8], Greg A. Valentine[1]

[1]Center for Geohazards Studies, University at Buffalo, Buffalo, NY, USA

[2] Department of Earth & Environmental Sciences, University of Missouri Kansas City, Kansas City, MO, USA

[3]Department of Physics and Astronomy, Brigham Young University, Provo, UT, USA

[4]Department of Earth Science and Earth Research Institute, University of California, Santa Barbara, CA, USA

[5]Istituto Nazionale di Geofisica e Vulcanologia, Rome, Italy

[6]Lamont Doherty Earth Observatory, Columbia University, Palisades, NY, USA

[7]Yamagata University, Yamagata, Japan

[8]Geological and Mining Engineering and Sciences, Michigan Tech, Houghton, MI, USA

Contents of this file

1. Figures S1 to S9
2. Tables S1, S2

Additional Supporting Information (Files uploaded separately)

1. Captions for Movies S1 to S4

Introduction

All data was collected during an NSF-funded workshop that focused on large scale experiments and volcanic hazards (Valentine & Sonder, 2018). Raw data, from which this article's results are derived is available in several datasets on VHub. A landing page there directs users to the respective parts (`vhub.org/resources/4710`, Sonder et al., 2021).

Figure S1.

Radial dependencies of wave forms of the seismo-acoustic dataset for pad 1. To make wave forme better visible, each channel was normalized to its RMS value before plotting.

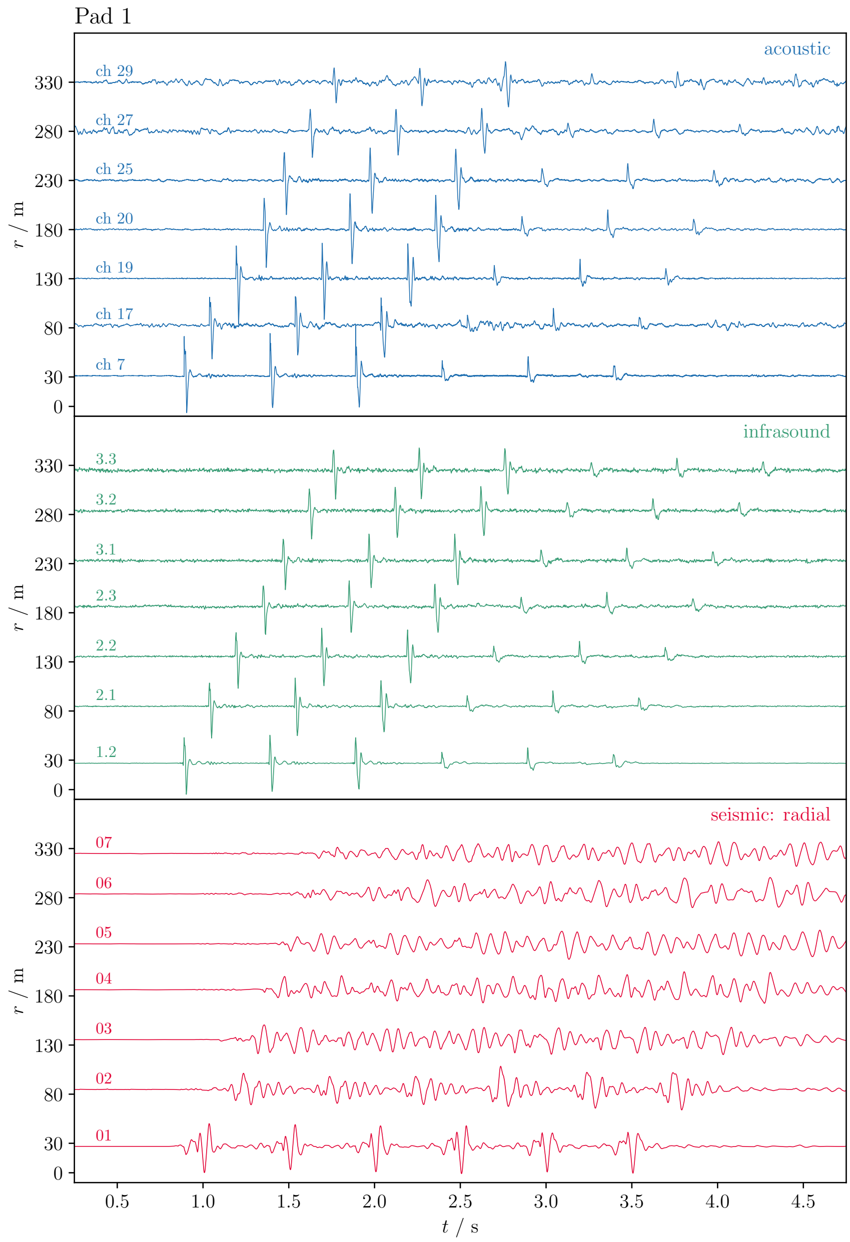

Figure S2.

Pad 2 radial wave form dependency. See description of Figure S1 and Figure 7 in the main text.

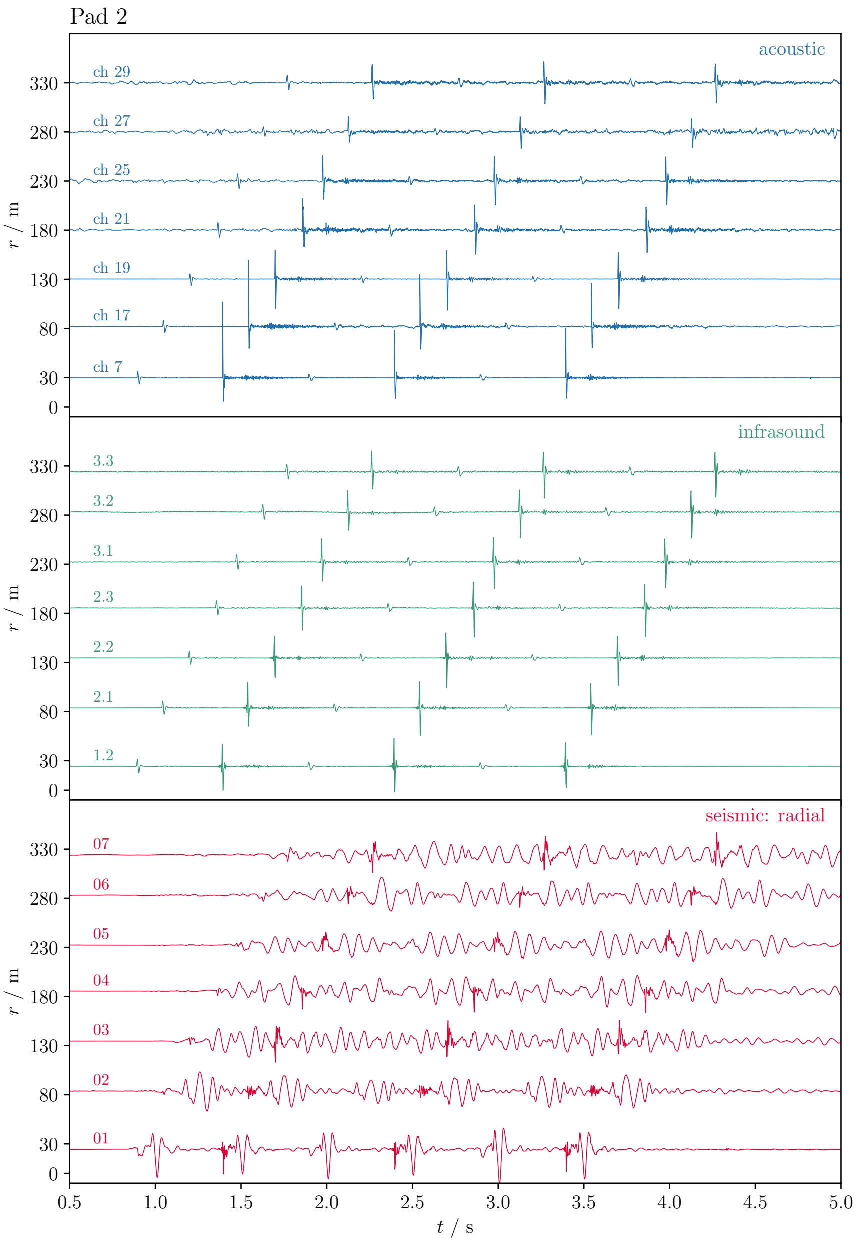

Figure S3.

Pad 3 radial wave form dependency. See description of Figure S1 and Figure 7 in the main text.

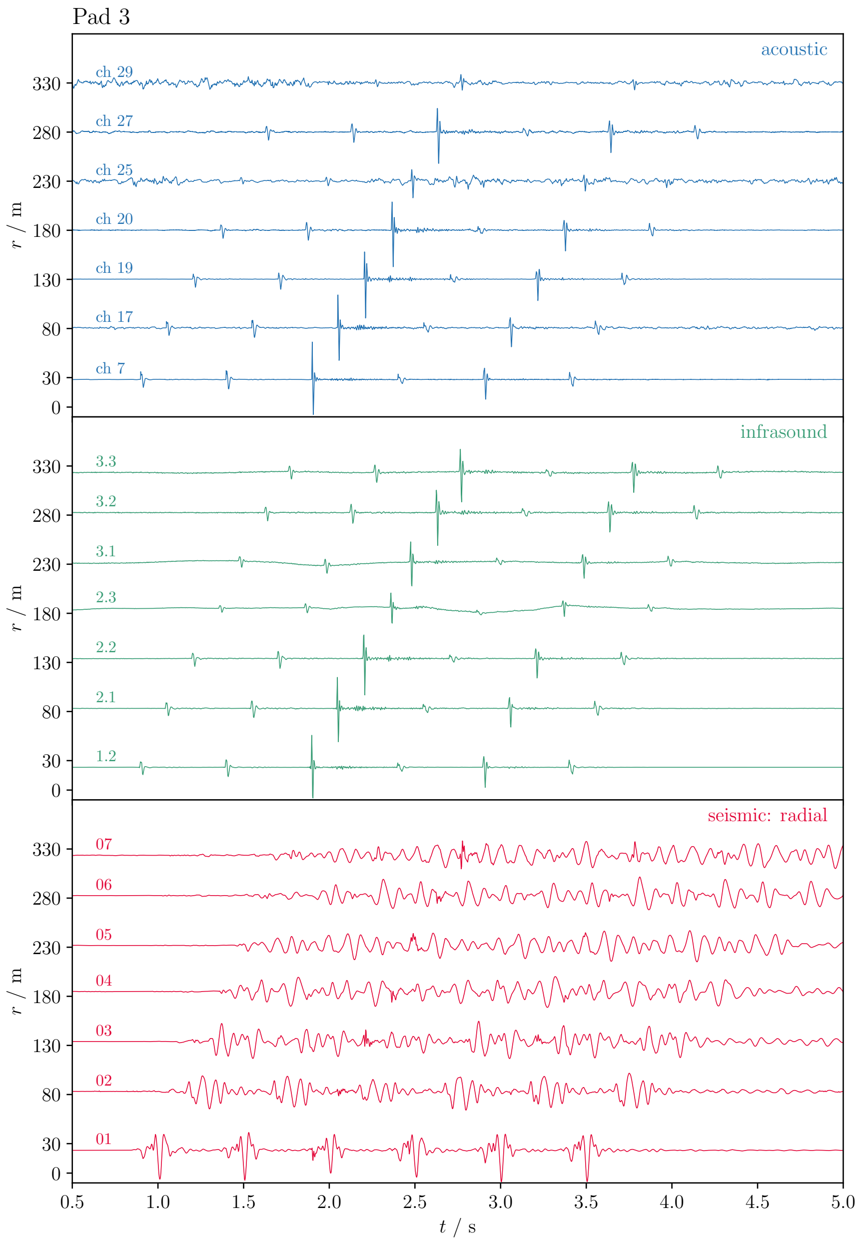

Figure S4.

Pad 4 radial wave form dependency. See description of Figure S1 and Figure 7 in the main text.

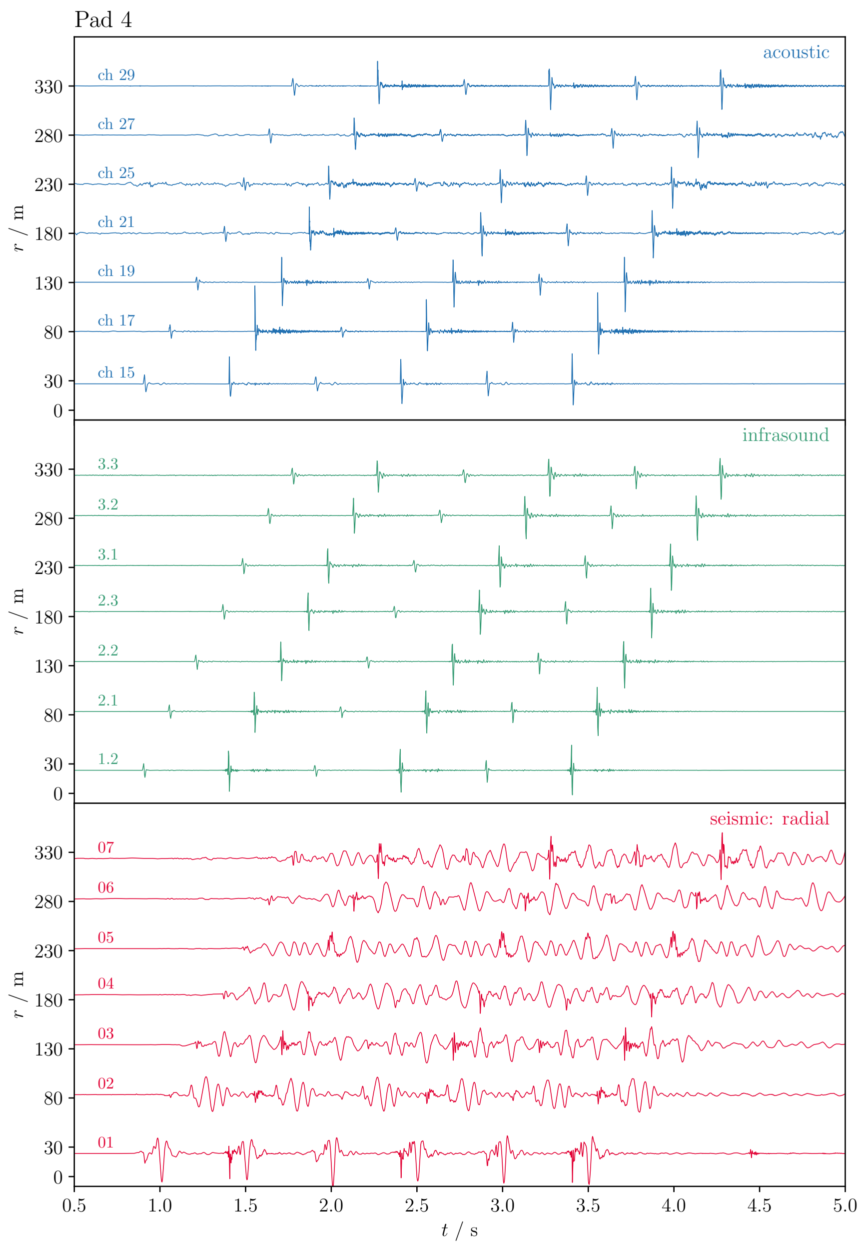

Figure S5.

Waveforms of airborne signals for increasing distances from source. For Pad 1 the upper charges were shot first, and they created larger pressure pulses. Blasts 1, 2 and 3 have relatively steep pressure onsets at closer range ($r \lesssim 100\,\mathrm{m}$). The $r = 130\,\mathrm{m}$ station recorded a relatively smooth waveform. At larger distances this shape seems to steepen again. The trends are consistent for all pads. They are, however most pronounced for blasts with high airborne signal.

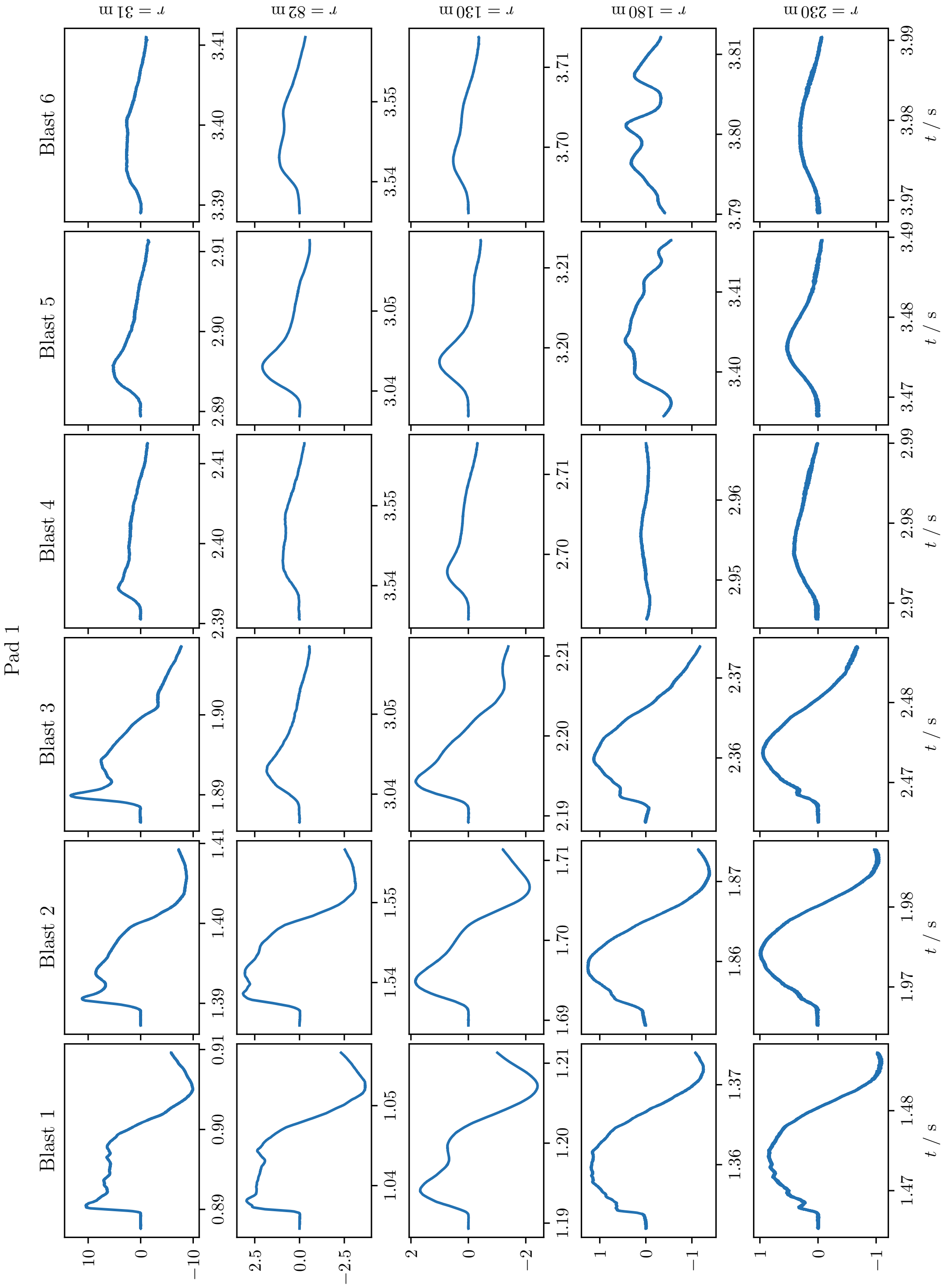
Pad 1
Blast 1
Blast 2
Blast 3
Blast 4
Blast 5
Blast 6
r = 31 m
r = 82 m
r = 130 m
r = 180 m
r = 230 m
p / Pa
t / s

34

Figure S6.

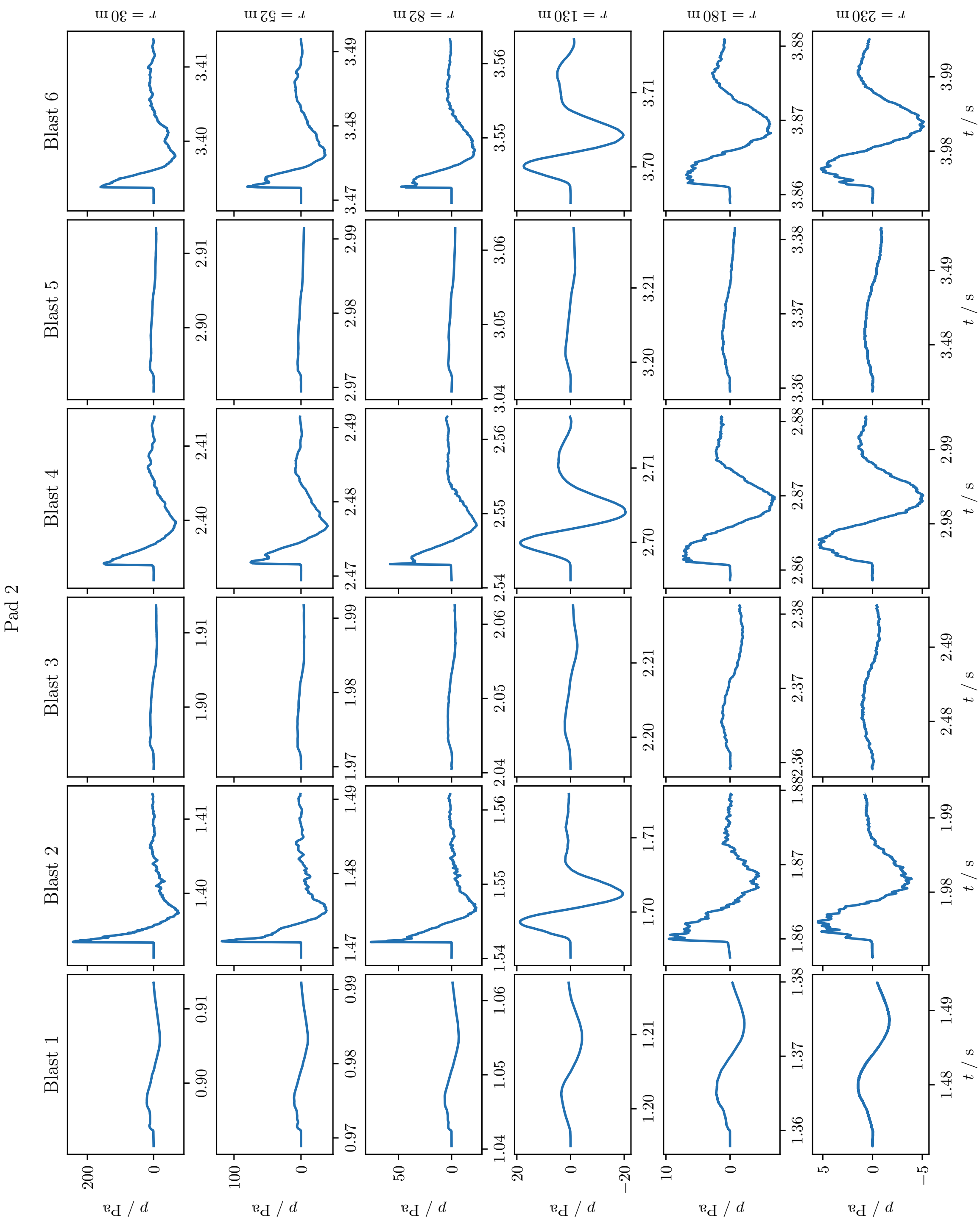

Pad 2
Blast 1
Blast 2
Blast 3
Blast 4
Blast 5
Blast 6
r = 30 m
r = 52 m
r = 82 m
r = 130 m
r = 180 m
r = 230 m
p / Pa
t / s

Figure S7.

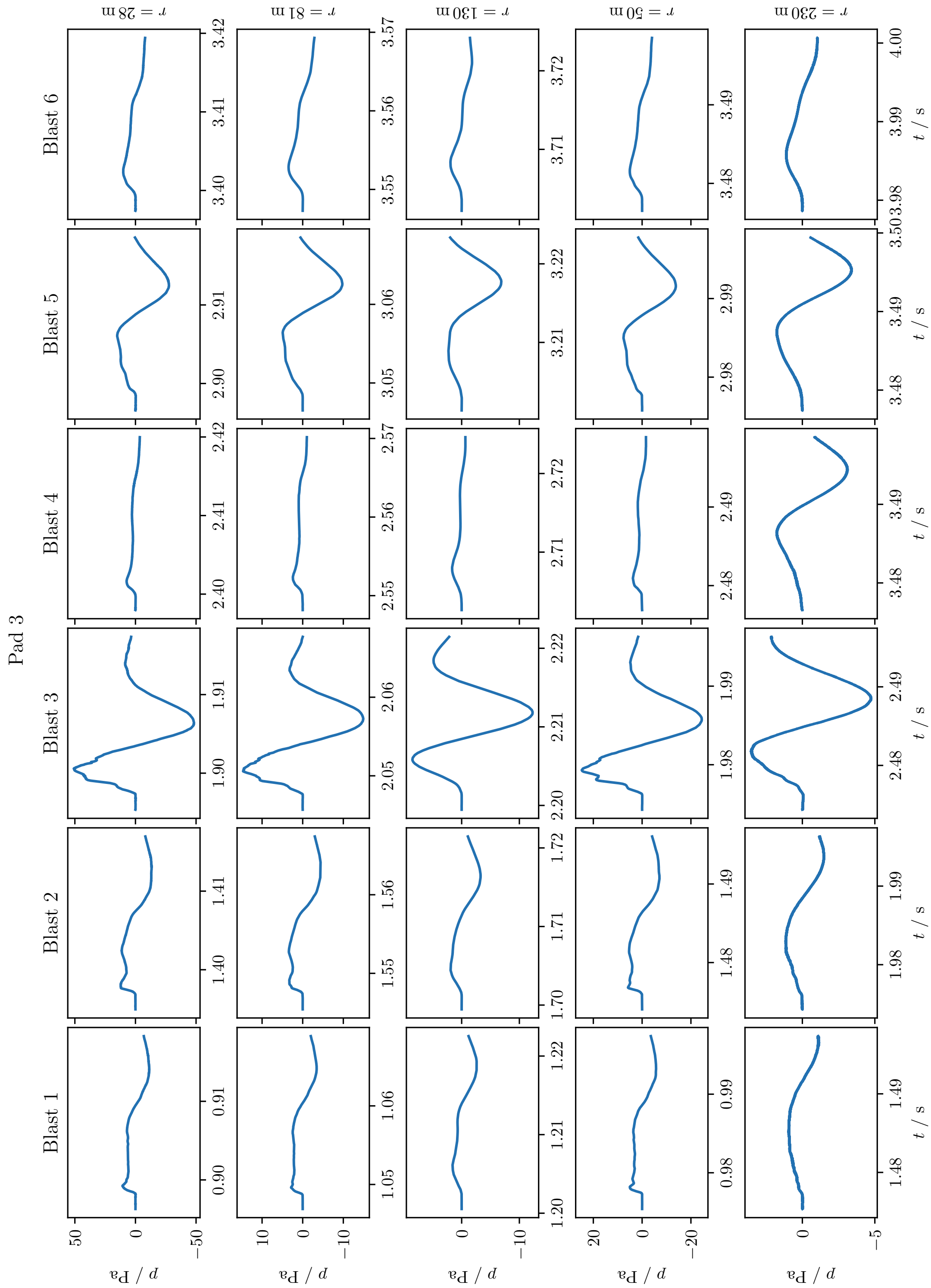
Pad 3
Blast 1
Blast 2
Blast 3
Blast 4
Blast 5
Blast 6
r = 28 m
r = 81 m
r = 130 m
r = 50 m
r = 230 m
p / Pa
t / s

Figure S8.

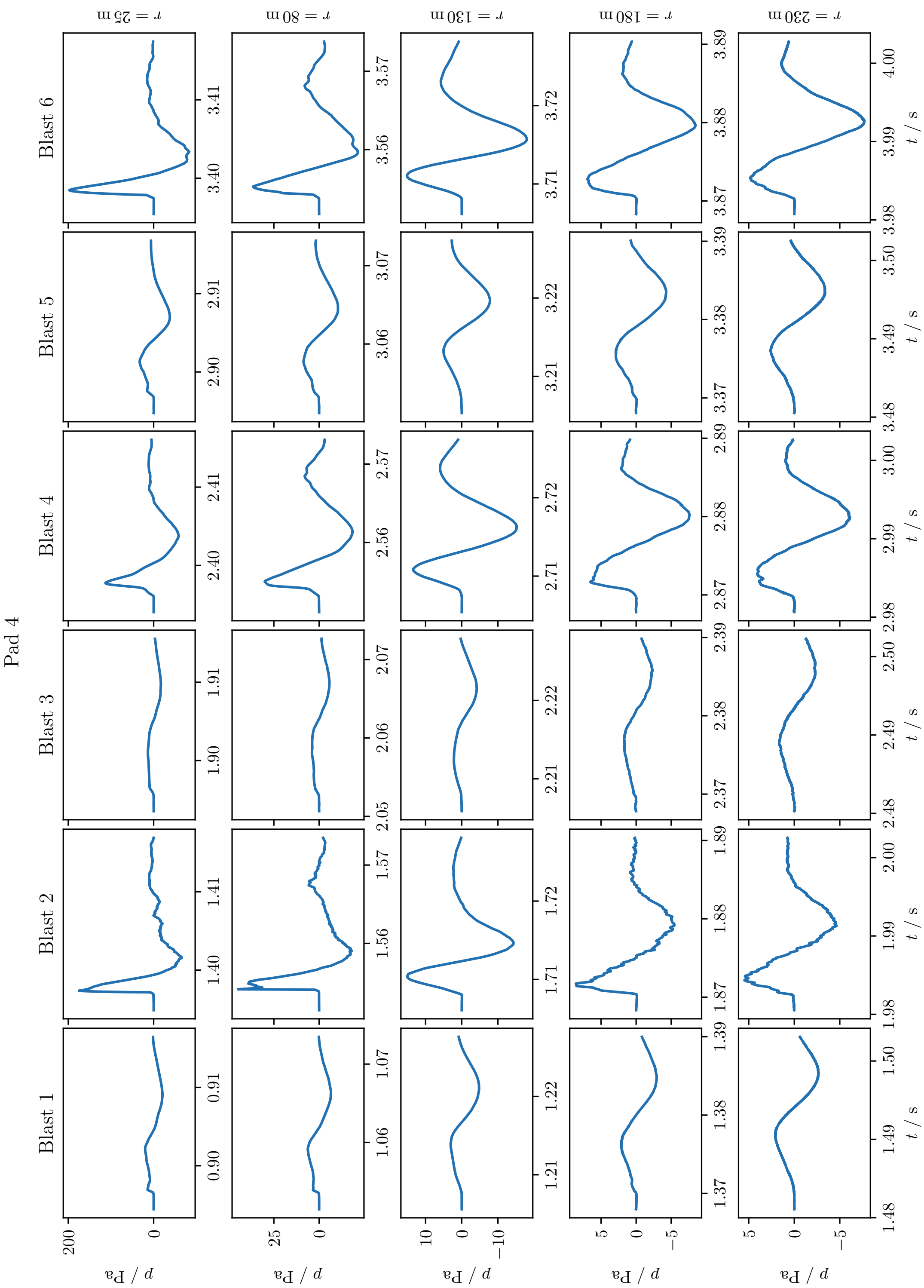
Pad 4
Blast 1
Blast 2
Blast 3
Blast 4
Blast 5
Blast 6
r = 25 m
r = 80 m
r = 130 m
r = 180 m
r = 230 m
p / Pa
t / s

Figure S9.

Squared airborne- and seismic signals at $r = 30\,\mathrm{m}$. The pads (2 and 4) with large airborne signals of blasts 1, 3 and 5 have smaller seismic signals for those blasts, when compared to the low-airborne signal blasts 2, 4 and 6 in the same pad.

For pad 2 squared airborne signals are roughly a factor 100 smaller compared to pads 2 and 4. In this case, the first three blasts produced the highest airborne *and* seismic values.

For pad 3 the airborne signal of blast 3 is highest and more than a factor 10 larger compared to pad 1 (blast 3). Seismic signal of that blast is reduced. Overall the seismic response for pad 3 is a factor 1.5 higher compared to all other pads. (Pad 3: all blasts peak $> 1.0 \times 10^{-6}\,\mathrm{m}^2\,\mathrm{s}^{-2}$, four of them $> 1.5 \times 10^{-6}\,\mathrm{m}^2\,\mathrm{s}^{-2}$. Other pads: just above $1.0 \times 10^{-6}\,\mathrm{m}^2\,\mathrm{s}^{-2}$) but typically below that level. This is the reason why the trend in Figure 11c of pad 3 is different that the other pads.

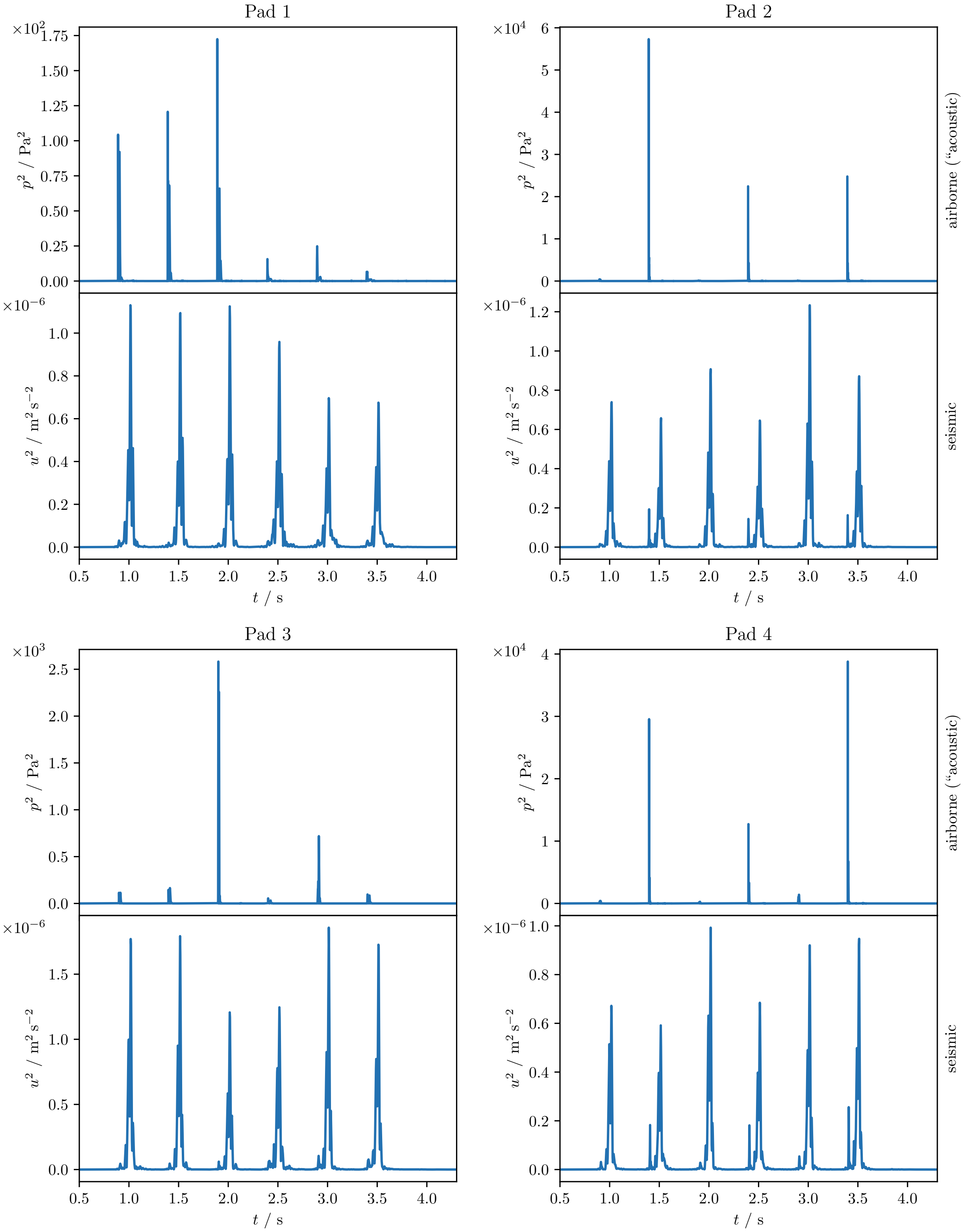

Pad 1
Pad 2
Pad 3
Pad 4
$\times 10^2$
$\times 10^4$
$\times 10^3$
$\times 10^{-6}$
p^2 / Pa^2
u^2 / m^2 s^{-2}
t / s
airborne ("acoustic)
seismic

57

Table S1.

Radial dependency of integrated, squared ground (particle) speed. F was determined from the radial dependency once for pads 1, 2 and 4, and another for pad 3.

Pad	Station	r (m)	$\int_0^\infty u_r^2\,dt$ ($\times 10^{-9}\,\mathrm{m^2\,s^{-1}}$)	F ($\times 10^{10}\,\mathrm{J\,s\,m^{-4}}$)
1	rad. 1	27	43	1.75
	rad. 3	135	1.2	
	rad. 4	186	0.73	
	rad. 5	233	0.66	
	rad. 6	284	0.24	
	rad. 7	325	0.14	
2	rad. 1	24	27	
	rad. 3	135	0.73	
	rad. 4	185	0.44	
	rad. 5	232	0.53	
	rad. 6	283	0.15	
	rad. 7	324	0.07	
3	rad. 1	23	68	0.55
	rad. 3	134	1.3	
	rad. 4	184	0.88	
	rad. 5	231	1.2	
	rad. 6	282	0.35	
	rad. 7	323	0.12	
	vert	29	33	
4	rad. 1	24	33	1.75
	rad. 3	134	0.71	
	rad. 4	185	0.45	
	rad. 5	232	0.75	
	rad. 6	282	0.18	
	rad. 7	323	0.06	
	vert	30	28	

Table S2.

Seismic energies E_s as determined from Equations 19 and 20. Values for $r^2 \int_{\Delta t} u_r^2 \, dt$ are listed for the two stations for which seismic per-blast signals did not overlap, which is the nearest radial station ('rad. stat. 1') and the vertical station ('vert. stat.'). The radial dependency (Equation 20, Table S1) provides values for F, so that ΔE can be determined from fitting a linear dependency to the per-blast ground motion. The E_s column results from

$$E_\mathrm{s} = F \, r^2 \int\limits_{\Delta t} u_r^2 \, dt \quad .$$

Pad	Blast	E_a (kJ)	$r^2 \int_{\Delta t} u_r^2\,dt$ rad. stat. 1 ($\times10^{-6}\,\mathrm{m^4\,s^{-1}}$)	$r^2 \int_{\Delta t} u_r^2\,dt$ vert. stat. ($\times10^{-6}\,\mathrm{m^4\,s^{-1}}$)	ΔE (kJ)	E_s (kJ)
1	1	4.32	5.62	–	79.7	98.5
	2	4.48	4.71	–		83.6
	3	3.88	5.26	–		92.3
	4	1.71	5.95	–		104.3
	5	2.59	4.55	–		79.9
	6	1.85	4.96	–		87.0
2	1	7.92	1.41	–		62.8
	2	32.6	3.58	–		46.3
	3	–	–	–		–
	4	33.4	2.64	–		47.5
	5	4.14	2.71	–		91.9
	6	28.9	5.24	–		62.3
3	1	6.42			35.5	29.8
	2	6.27	6.08	4.31		26.6
	3	16.1	4.02	3.48		18.9
	4	3.13	6.06	2.78		30.4
	5	6.79	6.75	4.90		31.7
	6	4.41	6.90	4.67		32.5
4	1	8.73	3.55	3.46	79.7	49.0
	2	23.6	2.82	2.77		55.5
	3	6.40	2.70	3.63		55.0
	4	25.2	3.31	2.96		59.1
	5	11.2	2.97	3.77		47.5
	6	28.8	2.90	2.51		78.4

Data Set S1.

Raw data is hosted on VHub (`https://vhub.org`) in standard formats. All raw data from which the presented analysis was derived was separated into five datasets.

1. Positions and coordinate systems (`https://vhub.org/resources/4793`).

2. Digital elevation models for the compound craters (`https://vhub.org/resources/4703`).

3. Broadband, high-frequency microphone records of the airborne signal (https://vhub.org/resources/4698).

4. Seismo-acoustic records (. . .).

5. Video material: Raw videos from which the supporting movies were created (https://vhub.org/resources/4801).

Movie S1–S4.

Annotated overview of each of the four blast sequences that were analyzed. One movie for each pad (i.e. blast configuration).

References

Sonder, I., Graettinger, A. H., Neilsen, T. B., Matoza, R. S., Taddeucci, J., Oppenheimer, J., . . . Valentine, G. A. (2021, September). *2018 NSF large scale experiment workshop with focus on volcanic blasts.* Retrieved from https://vhub.org/resources/4710

Valentine, G. A., & Sonder, I. (2018, December). Facilitating field-scale experiments in volcano hazards - Multidisciplinary Volcano Hazards Experiments at the Geohazards Field Station; Amherst and Springville, New York, 24–27 July 2018. *Eos*, *99*. doi: 10.1029/2018eo109237